
Demonstration of the Improved Rocket Efficiency in Direct-Drive Implosions by Using Different Ablator Materials

In direct-drive inertial confinement fusion (ICF), laser beams directly illuminate a fusion capsule.¹ The laser beams ablate the target surface and, through the rocket effect,² drive the capsule to velocities required for thermonuclear ignition. To achieve ignition conditions, the imploding shell must reach kinetic energy larger than a threshold value (E_{\min}) that depends strongly on the implosion velocity (maximum mass-averaged shell velocity), $E_{\min} \propto V_{\text{imp}}^{-6}$ (Ref. 3). To maximize the implosion velocity, the conversion of laser energy into kinetic energy of the shell (hydrodynamic efficiency) can be optimized by an appropriate choice of ablator material. By changing the ablator material, the rocket efficiency can be optimized (conversion of absorbed laser energy into kinetic energy of the shell). This article reports on the experimental investigation of the material dependence of the rocket efficiency in direct-drive implosions using the OMEGA laser.⁴

The rocket efficiency of ICF implosions depends on the drive pressure and mass ablation rate. To gain physical insight into the material dependence of these quantities, a stationary laser ablation model was used.⁵⁻⁷ The sound speed at the ablation region $[c_s \sim (I_L/\rho_A)^{1/3}]$ is given by balancing the energy flux of the laser (laser intensity I_L) with the energy flux of the plasma flow $\rho_A c_s^3$, where ρ_A is the mass density at the maximum laser absorption and c_s is the sound speed. Since the laser deposition region is given by the critical electron density, the mass density at the deposition region is given by $\rho_c = (\langle A \rangle / \langle Z \rangle) n_c m_p$, where ρ_c is the mass density at the critical density, n_c is the electron critical density, m_p is the mass of a proton, and $\langle A \rangle / \langle Z \rangle$ is the average atomic number over the average atomic mass. This shows that both the ablation pressure ($p_a \sim \rho_c c_s^2 \sim \rho_c^{1/3}$) and mass ablation rate ($m_a \sim \rho_c c_s \sim \rho_c^{2/3}$) increase with the ratio of $\langle A \rangle / \langle Z \rangle$. Although the model does not take into account some key physics of laser coupling, including the temperature dependence of laser deposition or cross-beam energy transfer (CBET),^{8,9} it predicts an increased rocket efficiency with increasing $\langle A \rangle / \langle Z \rangle$ in the ablator material.

Experimentally, the rocket efficiency is typically inferred by measuring the velocity of the target and using numerical

simulations to obtain the unablated target mass. Different techniques have been employed to measure the velocity of the shell in ICF experiments. Early planar experiments investigated the rocket efficiency using shadowgraphy and the peak x-ray emission from the coronal plasma.¹⁰⁻¹² In more-recent studies, time-averaged velocities were inferred from neutron bang-time measurements^{13,14} and time-resolved velocities have been determined using x-ray backlighting.¹⁵⁻¹⁸ In the direct-drive experiments, the absorbed energy has been varied by changing the intensity of the laser, the wavelength of the laser, the aspect ratio (thickness over the diameter of the shell) of the target, and the diameter of the laser beams relative to the target diameter.^{8,12-15} An extensive indirect-drive study of the implosion velocity was conducted at the National Ignition Facility, where the dopant material and dopant concentration were varied while maintaining a nearly constant $\langle A \rangle / \langle Z \rangle$ (Ref. 18).

This article describes the first demonstration of the effects of $\langle A \rangle / \langle Z \rangle$ on the hydrodynamic efficiency by measuring the implosion velocities for Be ($\langle A \rangle / \langle Z \rangle = 2.25$), C ($\langle A \rangle / \langle Z \rangle = 2$), and CH ($\langle A \rangle / \langle Z \rangle = 1.85$) ablators. A 20% increase in the velocity of the shell is measured for a Be ablator compared to CH and C ablators when maintaining a constant initial target mass. The hydrodynamic simulations of the time-resolved radius, velocity of the shell, and unabsorbed laser energy are in good agreement with the measurements. These results show an increase in hydrodynamic efficiency of 7% for C and 18% for Be over the CH ablator.

The experiments employed 60 OMEGA ultraviolet ($\lambda_0 = 351$ nm) laser beams that uniformly illuminated the target and were smoothed by polarization smoothing,¹⁹ smoothing by spectral dispersion,²⁰ and distributed phase plates [fourth-order super-Gaussian with a 650- μm full width at half maximum (FWHM)].²¹ Three 100-ps-long pickets were used to set the target implosion onto a low adiabat²² followed by a 1.2-ns square pulse that drove the target to its final velocity. The laser energy during the main drive was 22.9 ± 0.2 kJ, which resulted in an on-target overlapped intensity of 7×10^{14} W/cm². Three ablators (CH, C, and Be) were used with various mass densities

of 1.03 mg/cm^3 , 3.35 mg/cm^3 , and 1.83 mg/cm^3 corresponding to CH, C, and Be, respectively. Their thicknesses were varied to maintain the total ablator mass to be equivalent to $27\text{-}\mu\text{m}$ -thick CH. The outer radius was $447 \pm 10 \mu\text{m}$ and the total mass was $64 \pm 2 \mu\text{g}$.

The total unabsorbed laser energy was measured with an uncertainty of 5% using several calorimeters located around the target chamber. The scattered light was time resolved at four locations by multiplexing the signal into a 1.5-m spectrometer using a high-dynamic-range streak camera.²³ The system had a 100-ps (FWHM) temporal resolution.

The soft x rays (1 keV) emitted by the imploding target were imaged with a pinhole array ($10\text{-}\mu\text{m}$ -diam holes) onto a four-strip x-ray framing camera (XRFC) with a magnification of 12 (Ref. 24). This resulted in 16 time-resolved images (four per strip). Each image was time integrated over 40 ps. The relative timing between images (Δt) was known to $\sigma(\Delta t) \sim 5 \text{ ps}$ after off-line calibration using 10-ps x-ray bursts produced by the Multi-Terawatt laser.²⁵ The relative timing of the XRFC between shots was determined by measuring the electric pulse at the output of the microchannel plate relative to the laser fiducial. The absolute timing was determined by measuring the rise in x-ray emission relative to the laser fiducial. A 4-mm-diam gold target was irradiated with five

spatially distinct square laser beam pulses that rose over 100 ps to a 1-ns-long flattop [Fig. 136.1(a)]. An accuracy of 30 ps was determined from the standard deviation of several absolute timing measurements.

An accurate measurement of the position of the ablation surface was made using the steep inner edge [Fig. 136.1(b)] observed in the self-emission images [Fig. 136.1(c)]. This edge is created by the combination of the limb effect from the coronal soft x-ray emission and the absorption of the x rays, from the opposite side of the target, in the cold dense shell.²⁴ The absorption steepens the gradient by reducing the emission by a factor of 2 over a few microns in its direction. The position of the half-intensity point of this edge follows the radius, where the plasma temperature approaches zero (ablation surface) and provides an accurate measure of the radius of the shell. Since the peak-to-valley intensity is much larger than the noise, the position of the half-intensity point is not sensitive to it. The measurement accuracy of the position of the half-intensity point in the inner emission gradient for a single lineout is given by $(\text{MTF}/2) \times [1/(\text{S/N})] \approx 1 \mu\text{m}$, where $\text{MTF} = 10 \mu\text{m}$ is the modulation transfer function of the diagnostic and $\text{S/N} \sim 5$ is the signal-to-noise ratio, where the signal is given by the difference in the peak-to-valley. This accuracy is supported by the $3\text{-}\mu\text{m}$ standard deviation of the radius from the best-fit circle using a χ^2 analysis [insert in Fig. 136.1(b)]. The radius of

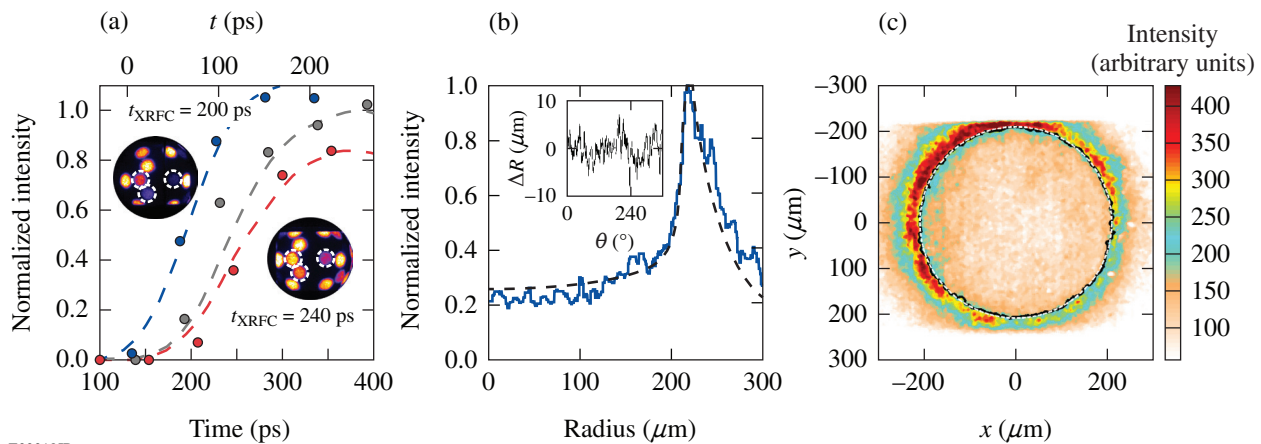


Figure 136.1

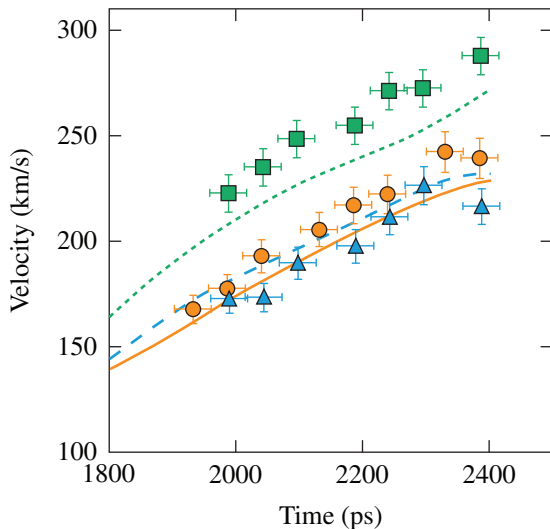
(a) A gold sphere is illuminated by several laser beams that are delayed with successive 50-ps intervals. To absolutely calibrate the timing of the x-ray framing camera (XRFC) to the laser, the x-ray emission measured by the XRFC, in the time reference (bottom axis) of the XRFC (symbols), is compared to the measured laser pulse, in the time reference (top axis) of the laser (curves). The two images (insets) correspond to the XRFC measurements at $t_{\text{XRFC}} = 200 \text{ ps}$ and $t_{\text{XRFC}} = 240 \text{ ps}$. The dashed white circles correspond to the three beams used in the plot. (b) A single radial lineout (solid curve) of the self-emission image is compared with a lineout obtained from post-processing the hydrodynamic simulation (dashed curve). The variation of the difference between the half-intensity point and the radius of the best circle is plotted (inset). (c) The self-emission image at $t = 2.5 \text{ ns}$ was obtained from a CH target. The black curve corresponds to the location of the half-intensity point; the dashed white circle corresponds to the best-fit circle.

the shell, at each time, was obtained by averaging the position of the inner gradient over angle. This improved the accuracy by a factor of $\sqrt{N} \approx 10$, where $N = 2\pi R/\text{MTF}$ is the number of independent measurements and R is the radius from the χ^2 analysis. This results in a radial measurement accuracy of $\sigma(R) < 0.4 \mu\text{m}$. The accuracy in the measurement of the averaged ($\Delta t = 200$ ps) velocity is given by

$$\frac{\sigma(V)}{V} = \sqrt{\left[\frac{\sigma(\Delta t)}{\Delta t}\right]^2 + \left[\frac{\sigma(\Delta R)}{\Delta R}\right]^2} \approx 4\%, \quad (1)$$

where, for a velocity of 200 km/s, $\Delta R = 40 \mu\text{m}$ and $\sigma(\Delta R) = \sqrt{2}\sigma(R) = 0.6 \mu\text{m}$.

Figure 136.2 shows that, for all times, the velocity of the shell is higher in the Be ablator than in the CH and C ablaters. The velocity increases in time to ~ 240 km/s for the CH, ~ 230 km/s for the C, and ~ 290 km/s for the Be ablator. A 20% increase in the velocity of the shell was measured at the end of the laser pulse when a Be ablator was used rather than the standard CH or C ablator. This increase is a result of the increase in $\langle A \rangle / \langle Z \rangle$ for Be compared to C and CH.



E22220JR

Figure 136.2
Comparison of the calculated (curves) and measured velocities of the shells averaged over 200 ps (symbols) in CH (orange solid line and circles), C (blue dashed line and triangles), and Be (green dotted line and squares) ablaters. Timing error bars correspond to the absolute timing; the relative timing between points is smaller (5 ps).

Figures 136.3(a)–136.3(c) show the time-resolved radii of the imploding shell for the three ablaters. An excellent reproduc-

ibility in trajectory measurements was observed by repeating the shots (two times for C and three times for Be). A decoupling between the position of the shell and the measured radius from the self-emission images occurred at the end of the laser pulse when the plasma was no longer being heated. This reduced the plasma expansion velocity, increasing the plasma density on the outside of the shell.

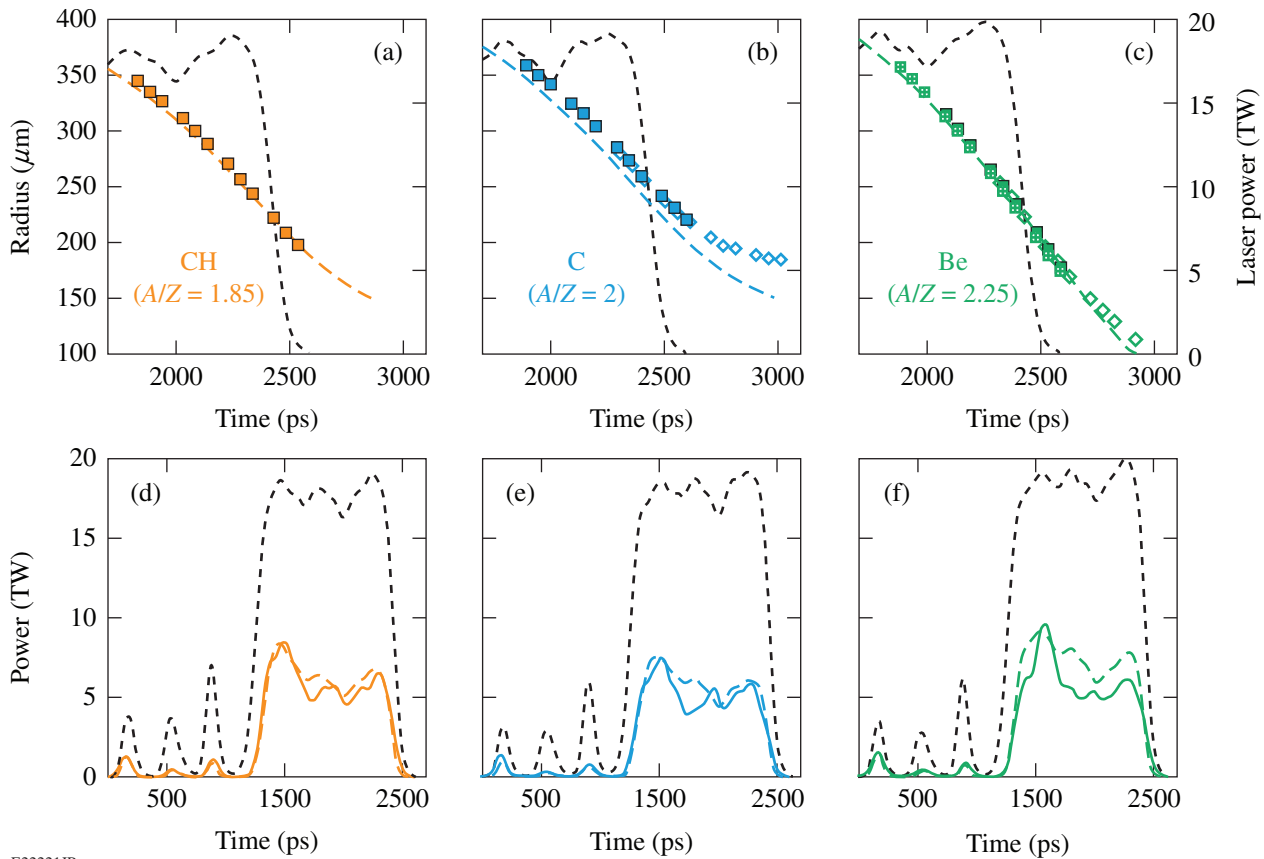
Simulations of the trajectories [Figs. 136.3(a)–136.3(c)] and velocities (Fig. 136.2) of the shells are in good agreement with measurements, indicating that the ablation pressure P_a and the mass M of the shell are well modeled:

$$\left(\frac{P_a}{M} = \frac{1}{4\pi R^2} \frac{dV}{dt}\right). \quad (2)$$

This suggests that the coupling of the absorbed laser energy to the shell motion is well modeled. The 80-ps delay observed in the C trajectories [Fig. 136.3(b)] and velocities (Fig. 136.2) may be caused by a delay in the arrival of the shock at the inner interface of the shell, leading to a delay in the initial target motion and indicating an error in the equation of state for C.

The measured shell trajectories were compared with hydrodynamic simulations by post-processing simulations with *Spect3D*²⁶ and extracting the position of the half-intensity point at each time in the calculated self-emission profile. Simulations included both nonlocal heat transport²⁷ and CBET models⁹ developed in the 1-D hydrodynamic code *LILAC*.²⁸ Simulated images were integrated over 40 ps and convolved by the MTF of the diagnostic. The comparison of the measured and calculated emission profiles displayed in Fig. 136.1(b) shows that the gradients of the inner edge are in excellent agreement. The position of the inner surface is insensitive to the models used since it is dominated by the point where the temperature approaches zero (a well-defined point in the simulations) and does not require Abel inversion for comparison with the simulations. The half-intensity point follows the ablation front with a constant difference of $3.5 \mu\text{m}$ caused by the widening of the inner edge by the convolution with the MTF of the diagnostic.

Figures 136.3(d)–136.3(f) show the time-resolved unabsorbed laser light measurements for the three ablaters. The total absorption was measured to be 69% for Be and CH, increasing to 72% for C. This indicates that the increase in implosion velocity for the Be ablator is a result of increased conversion efficiency of the absorbed energy into kinetic energy, not an increase in the absorption. There is excellent agree-



E22221JR

Figure 136.3

[(a)–(c)] Comparison of the calculated (curves) and measured (symbols) shell trajectories (the different symbols represent different shots). [(d)–(f)] Comparison of the measured (solid curve) and calculated (dashed curve) unabsorbed scattered light. The results are presented for [(a) and (d)] CH, [(b) and (e)] C, and [(c) and (f)] Be ablaters. The laser power is plotted on each figure (dashed black curve) and corresponds to an on-target overlapped intensity of 7×10^{14} W/cm².

ment between the simulated and measured unabsorbed laser powers for C and CH ablaters, which is consistent with the good agreement in shell velocities (Fig. 136.2). This indicates that when both nonlocal heat transport and CBET are included, the simulations correctly account for the absorption of the laser energy. For the Be ablator, the calculated total absorption is slightly smaller (60%) than in the experiments, which is consistent with the slightly lower (6% lower) calculated velocities.

Figure 136.4 shows the results from simulations where the ablation pressure increases and the percentage of remaining mass decreases with increasing $\langle A \rangle / \langle Z \rangle$. This produces a higher acceleration of the shell, at a given radius, leading to a higher implosion velocity for Be. In higher-energy designs, the longer acceleration phase will likely increase the velocity of the shell in Be more than what is measured in these experiments.

The increased ablation pressure, combined with the higher mass ablation rate, leads to a higher kinetic energy and hydro-

dynamic efficiency [Fig. 136.4(c)]. The hydrodynamic efficiency was calculated to be increased by 18% for Be and 7% for C compared to the CH ablator. In these experiments, the simulation slightly underestimates the hydrodynamic efficiency for Be since the laser absorption [Fig. 136.3(f)] and the shell velocity (Fig. 136.2) were measured to be slightly higher than calculated by the simulations. The transfer of absorbed laser energy into the kinetic energy (rocket efficiency) of the shell was calculated to increase by 28% for Be and 5% for C ablaters compared to the CH ablator.

In summary, a 20%-higher implosion velocity was obtained when using a Be ablator compared to a C or CH ablator. Simulations that include nonlocal heat transport and CBET models accurately reproduce shell trajectories, velocities, and unabsorbed laser power for the three materials. They show that the increase in velocity is a result of increasing $\langle A \rangle / \langle Z \rangle$ and that the hydrodynamic efficiency is increased by 18% for Be and 7% for C ablaters over a CH ablator.

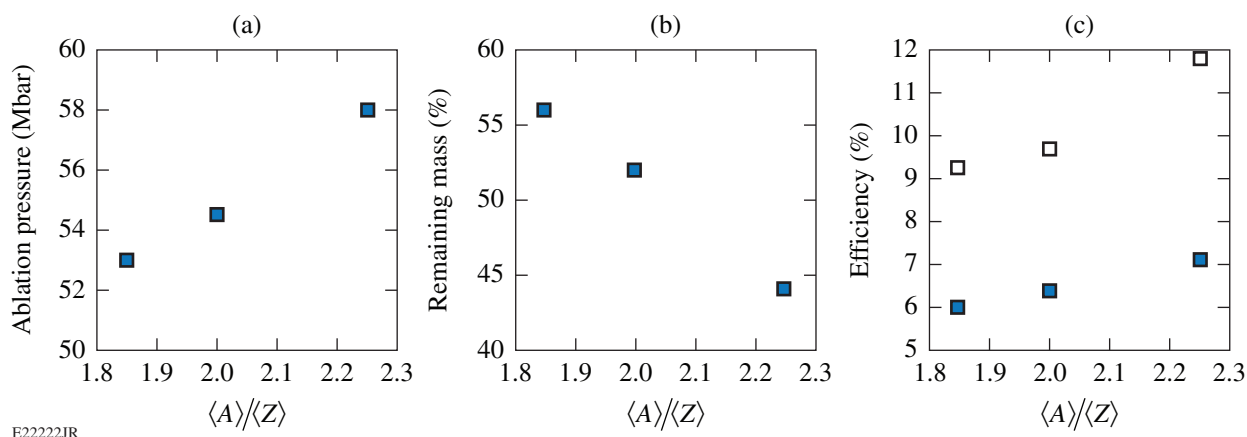


Figure 136.4

Comparison of the calculated (a) ablation pressure and (b) percentage of remaining mass at $t = 2.3$ ns for the CH ablator ($\langle A \rangle / \langle Z \rangle = 1.85$), C ablator ($\langle A \rangle / \langle Z \rangle = 2$), and Be ablator ($\langle A \rangle / \langle Z \rangle = 2.25$). (c) Comparison of the hydrodynamic efficiency (solid squares) and the efficiency of the transfer of the absorbed laser into the kinetic energy of the shell (open squares) for the three ablators.

ACKNOWLEDGMENT

This work was supported by the U.S. Department of Energy Office of Inertial Confinement Fusion under Cooperative Agreement No. DE-FC52-08NA28302, the University of Rochester, and the New York State Energy Research and Development Authority. The support of DOE does not constitute an endorsement by DOE of the views expressed in this article.

REFERENCES

1. J. Nuckolls *et al.*, *Nature* **239**, 139 (1972).
2. M. Murakami and K. Nishihara, *Jpn. J. Appl. Phys.* **26**, 1132 (1987).
3. M. C. Herrmann, M. Tabak, and J. D. Lindl, *Nucl. Fusion* **41**, 99 (2001).
4. T. R. Boehly, D. L. Brown, R. S. Craxton, R. L. Keck, J. P. Knauer, J. H. Kelly, T. J. Kessler, S. A. Kumpan, S. J. Loucks, S. A. Letzring, F. J. Marshall, R. L. McCrory, S. F. B. Morse, W. Seka, J. M. Soures, and C. P. Verdon, *Opt. Commun.* **133**, 495 (1997).
5. W. M. Manheimer, D. G. Colombant, and J. H. Gardner, *Phys. Fluids* **25**, 1644 (1982).
6. P. Mora, *Phys. Fluids* **25**, 1051 (1982).
7. C. E. Max, C. F. McKee, and W. C. Mead, *Phys. Fluids* **23**, 1620 (1980).
8. D. H. Froula, I. V. Igumenshchev, D. T. Michel, D. H. Edgell, R. Follett, V. Yu. Glebov, V. N. Goncharov, J. Kwiatkowski, F. J. Marshall, P. B. Radha, W. Seka, C. Sorce, S. Stagnitto, C. Stoeckl, and T. C. Sangster, *Phys. Rev. Lett.* **108**, 125003 (2012).
9. I. V. Igumenshchev, W. Seka, D. H. Edgell, D. T. Michel, D. H. Froula, V. N. Goncharov, R. S. Craxton, L. Divol, R. Epstein, R. Follett, J. H. Kelly, T. Z. Kosc, A. V. Maximov, R. L. McCrory, D. D. Meyerhofer, P. Michel, J. F. Myatt, T. C. Sangster, A. Shvydky, S. Skupsky, and C. Stoeckl, *Phys. Plasmas* **19**, 056314 (2012).
10. R. Decoste *et al.*, *Phys. Rev. Lett.* **42**, 1673 (1979).
11. B. H. Ripin *et al.*, *Phys. Plasmas* **23**, 1012 (1980).
12. D. T. Attwood *et al.*, *Phys. Rev. Lett.* **38**, 282 (1977).
13. T. H. Tan *et al.*, *Phys. Fluids* **24**, 754 (1981).
14. P. B. Radha, C. Stoeckl, V. N. Goncharov, J. A. Delettrez, D. H. Edgell, J. A. Frenje, I. V. Igumenshchev, J. P. Knauer, J. A. Marozas, R. L. McCrory, D. D. Meyerhofer, R. D. Petrasso, S. P. Regan, T. C. Sangster, W. Seka, and S. Skupsky, *Phys. Plasmas* **18**, 012705 (2011).
15. M. H. Key *et al.*, *Opt. Commun.* **44**, 343 (1983).
16. B. A. Hammel *et al.*, *Phys. Fluids B* **5**, 2259 (1993).
17. D. G. Hicks, B. K. Spears, D. G. Braun, R. E. Olson, C. M. Sorce, P. M. Celliers, G. W. Collins, and O. L. Landen, *Phys. Plasmas* **17**, 102703 (2010).
18. D. G. Hicks *et al.*, *Phys. Plasmas* **19**, 122702 (2012).
19. T. R. Boehly, V. A. Smalyuk, D. D. Meyerhofer, J. P. Knauer, D. K. Bradley, R. S. Craxton, M. J. Guardalben, S. Skupsky, and T. J. Kessler, *J. Appl. Phys.* **85**, 3444 (1999).
20. S. Skupsky, R. W. Short, T. Kessler, R. S. Craxton, S. Letzring, and J. M. Soures, *J. Appl. Phys.* **66**, 3456 (1989).
21. T. J. Kessler, Y. Lin, J. J. Armstrong, and B. Velazquez, in *Laser Coherence Control: Technology and Applications*, edited by H. T. Powell and T. J. Kessler (SPIE, Bellingham, WA, 1993), Vol. 1870, pp. 95–104.
22. V. N. Goncharov, T. C. Sangster, T. R. Boehly, S. X. Hu, I. V. Igumenshchev, F. J. Marshall, R. L. McCrory, D. D. Meyerhofer, P. B. Radha, W. Seka, S. Skupsky, C. Stoeckl, D. T. Casey, J. A. Frenje, and R. D. Petrasso, *Phys. Rev. Lett.* **104**, 165001 (2010).

23. W. R. Donaldson, R. Boni, R. L. Keck, and P. A. Jaanimagi, *Rev. Sci. Instrum.* **73**, 2606 (2002).
24. D. T. Michel, C. Sorce, R. Epstein, N. Whiting, I. V. Igumenshchev, R. Jungquist, and D. H. Froula, *Rev. Sci. Instrum.* **83**, 10E530 (2012).
25. V. Bagnoud, I. A. Begishev, M. J. Guardalben, J. Puth, and J. D. Zuegel, *Opt. Lett.* **30**, 1843 (2005).
26. J. J. MacFarlane *et al.*, *High Energy Density Phys.* **3**, 181 (2007).
27. V. N. Goncharov, T. C. Sangster, P. B. Radha, R. Betti, T. R. Boehly, T. J. B. Collins, R. S. Craxton, J. A. Delettrez, R. Epstein, V. Yu. Glebov, S. X. Hu, I. V. Igumenshchev, J. P. Knauer, S. J. Loucks, J. A. Marozas, F. J. Marshall, R. L. McCrory, P. W. McKenty, D. D. Meyerhofer, S. P. Regan, W. Seka, S. Skupsky, V. A. Smalyuk, J. M. Soures, C. Stoeckl, D. Shvarts, J. A. Frenje, R. D. Petrasso, C. K. Li, F. Séguin, W. Manheimer, and D. G. Colombant, *Phys. Plasmas* **15**, 056310 (2008).
28. J. Delettrez, *Can. J. Phys.* **64**, 932 (1986).